Nanoscale

PAPER

View Article Online
View Journal | View Issue

Cite this: *Nanoscale*, 2020, **12**, 22639

Quantification of surface composition and segregation on AuAg bimetallic nanoparticles by MALDI MS†

Suiyang Liao, [a] Zhi Luo, [a] Jonas Bastian Metternich,[b] Renato Zenobi[b] and Francesco Stellacci *[a,c]

Received 6th July 2020,
Accepted 2nd November 2020

DOI: 10.1039/d0nr05061j

rsc.li/nanoscale

In this work we show that it is possible to use MALDI-TOF as a tool to quantify the atomic composition and to describe the phase segragation of the surface of ligand-coated, bimetallic AuAg nanoparticles. Our investigation shows that AuAg nanoparticles of various compositions exhibit core–shell heterogeneity with surface enrichment of Ag. A Monte-Carlo type simulation demonstrates that the surface Au and Ag atoms arrange in a random fashion.

Introduction

Bimetallic nanoparticles (BMNPs) are an important class of material that has found wide applications in electrocatalysis,[1,2] biosensing[3,4] and optical devices.[5,6] The synergistic interplay between two different metal elements is one of the keys to the unique properties of the BMNPs. It has been well documented that both the composition as well as the alloying/segregation patterns of the metal mixtures are essential in determining their properties.[1,7–9] For example, Suntivich *et al.* demonstrated a direct correlation between the surface composition of Au–Pt BMNPs and their catalytic activities.[7] Likewise, the catalytic performance of AuAg BMNPs was found to be ideal at a 25% Au surface coverage.[8] It is also noteworthy that, while it has been proven to be beneficial to alloy Pt with other transition metals for improved activity and stability, continuous surface segregation can occur for PtCo BMNPs under certain conditions.[9] In most of these cases, special attention has been paid to the surface structures of the BMNPs, as most of the molecular interactions under reactive conditions happen at the interface. Therefore, it is of paramount importance to thoroughly characterize the interfacial structures of these NPs.[10–17]

To date, while a plethora of techniques have been utilized for BMNPs achieving high spatial and chemical resolution, precise quantification and morphological description of the outmost atomic layer of bimetallic nanoparticles remains a challenge especially for ensemble measurement.[18] X-ray diffraction (XRD) pattern are performed to track atomic ordering by probing lattice constants.[15] X-ray photoelectron spectroscopy (XPS), from a binding energy point of view, is used to quantitatively relate the interface area of CuAg nanodimers to the Ag3d peak shift.[15,19] Extended X-ray absorption fine structure spectroscopy (EXAFS) has been utilized to confirm the surface enrichment of Ag in AuAg bimetallic NPs[20] and the potential of the experimental data can be further exploited with Monte Carlo simulation and supervised machine learning to elucidate more structural subtleties, such as coordination number[21] and partial radial distribution.[22] However, X-ray based techniques cannot easily characterize the distribution of atoms on the surface of nanoparticles. Tools from the family of electron microscopy are also widely applied to BMNP characterization. High-resolution transmission electron microscopy (HRTEM), relying on the contrast difference between various phases, allows for direct imaging of atomic structures.[16] Taking advantage of the contrast due to various atomic numbers, high-angle annular dark-field imaging (HAADF) differentiates elements by their electron-scattering ability, but this technique alone cannot provide sufficient information to identify elements.[15,16,19,23,24] Thus, energy-probing tools, such as electron energy loss spectroscopy (EELS) and energy-dispersive X-ray spectroscopy (EDX), are often coupled with HAADF for compositional analysis.[8,15,16,23,24] However, these approaches provide information only on a few nanoparticles, often the easiest to image, leaving a strong need for ensemble characterizing tools to support their findings.

Previously, MALDI has been developed to characterize the composition and morphology (*i.e.* phase segregation) of binary

[a]*Institute of Materials, École Polytechnique Fédérale de Lausanne, Station 12, 1015 Lausanne, Switzerland. E-mail: francesco.stellacci@epfl.ch*
[b]*Department of Chemistry and Applied Biosciences, ETH Zurich, CH-8093 Zurich, Switzerland*
[c]*Interfaculty Bioengineering Institute, École Polytechnique Fédérale de Lausanne, Station 12, 1015 Lausanne, Switzerland*

†Electronic supplementary information (ESI) available. See DOI: 10.1039/d0nr05061j

mixtures of ligand molecules on Au or Ag nanoparticles.[25–33] Initially, MALDI, coupled with ion mobility-MS, was used to analyze Au-thiolate complexes desorbed from the nanoparticles. These complexes were interpreted as being composed of surface Au atoms that had desorbed together with the thiolated ligands that were originally attached to them. The composition of the complexes was used to determine the composition of the ligand shell.[25] With the assumption that a random distribution of ligands will lead to a binomial probability distribution of compositions in the fragment signals, Dass *et al.* studied ligand exchange of Au_{25} clusters.[27] Harkness *et al.* experimentally developed further this assumption by studying larger Au nanoparticles and focusing on the mass distribution of the most abundant $Au_4L^A_{4-x}L^B_x$ complexes (with x being an integer and $0 \leq x \leq 4$). They showed that a statistical distance (sum of squared residuals, SSR) between the experimental distribution of the abundancy of the five possible fragments and the reference theoretical one (binomial distribution) could be used to determine whether the distribution of ligands in the ligand shell was random (minimal distance from the theoretical distribution), patchy (medium distance), or Janus (maximum distance). They tested this hypothesis on particles coated with octanethiol (OT) and deuterated [D17]OT as ligands, showing an experimental distribution of the possible fragments that was extremely close to the expected binomial one. They analysed nanoparticles coated with a wide variety of binary thiols and found all possible surface nanophase morphologies.[26] The same phenomenon was also reported on Ag nanoparticles.[29,31,34] Our group applied this technique to characterize the evolution of the ligand-shell's morphology during a ligand exchange reaction for Au nanoparticles.[32] We then further improved the characterization of the ligand shell by developing a Monte-Carlo-type simulation capable of reconstructing a model of the ligand shell morphology and provide a distribution of nearest neighbors. The method is based on simultaneous fitting of all residues not just an analysis of the most abundant ones. The results obtained were validated by comparison with SANS and NMR.[33]

In summary, when MALDI-TOF is used on Au or Ag nanoparticles one obtains $M_nL^A_{m-x}L^B_x$ complexes (with M being Au or Ag, n being an integer typically between 2 and 8, and x being an integer between 0 and m; $m = n$ or $n + 1$ depending on the metal). The study of these fragments has been very effective for the characterization of the ligand shell in terms of composition and morphology. Herein, we show that MALDI-TOF MS can be used to characterize the first atomic layers of AuAg bimetallic nanoparticle both for the composition and for the surface morphology (*i.e.* the segregation pattern). In other words, we show that the fragments produced in MALDI-TOF can be used to characterize the surface atoms when all parameters on the ligand shell are known. Specifically, in this work, AuAg nanoparticles covered with 1-dodecanthiol (DDT) were synthesized and used as a model system to prove the concept. We find that, when irradiated by the MALDI laser, these DDT-capped AuAg NPs generate fragments that can be described according to the chemical formula, $(Au_xAg_{n-x})L_{n-1}$ (L denoting the ligands, with x being an integer and $0 \leq x \leq n$). Given the body of work on this technique achieved to date, it is safe to assume that the Ag and Au atoms present in the fragment are the surface atoms of the nanoparticles. Consequently, these particles' surface composition can be derived directly by a quantitative analysis of the atom abundance in the mass spectral fragments. This can be done globally for all of the fragments under all n, as well as separately for each groups of the fragments that share a common n. The results calculated from different n exhibit very good consistency with each other and with the global results. Importantly with the data achieved it is possible to perform a morphological analysis using the fragmentation pattern. In this paper, this was done both using SSR and Monte Carlo-type simulations. To the best of our knowledge, this is the first time that MALDI MS has been applied to investigate surface atomic composition of bimetallic particles.

Results and discussion

We synthesized particles using a co-reduction of Au(III) and Ag (I) cations in the presence of DDT, based on the principle of Stucky method.[35] The synthesis yielded thiolated AuAg NPs with a diameter in the range of 2–4 nm. The particles produced are summarized in Table 1 (Synthesis and purification are described in details in the Experimental section; representative TEM images in Fig. S1†.) The size distribution of the particles was characterized using TEM images. The images were analyzed by using a tailor-made macro automation on ImageJ.

We then characterized all particles using MALDI-TOF. We found that two matrix materials, *trans*-2-[3-(4-*tert*-butylphenyl)-2-methyl-2-propenylidene]malononitrile (DCTB) and 9-nitroanthracene (9-NA), facilitated the ionization process. With the simple dried droplet sample preparation method (details in Experimental), around 3 μl of the mixture of DDT AuAg NPs and matrix material were pipetted onto the MALDI target and dried together to form an analyte spot.[36] The MALDI laser breaks the nanoparticles' surface into ionized fragments as illustrated in Fig. 1A. Fig. 1B shows one of the mass spectra under the m/z (mass/charge) detection window from ~600 to 2600. Benefiting from the good mass accuracy (<200 ppm) and resolution of reflectron mode (~10 000), the correct assign-

Table 1 Summary of the AuAg NPs used in this work (the errors in TEM sizing and MALDI quantification are expressed as 1 SD = Standard deviation)

Sample	Au% feed	Diameter by TEM	Au% MALDI	Au% ICP	Au% XPS
A	10	2.9 ± 0.7	13.9 ± 1.2	24	30
B	20	2.4 ± 0.6	11.2 ± 1.7	28	31
C	30	3.0 ± 0.9	23.0 ± 0.7	41	47
D	40	3.8 ± 1.1	46.8 ± 1.3	53	43
E	50	3.6 ± 0.9	30.4 ± 0.4	32	35

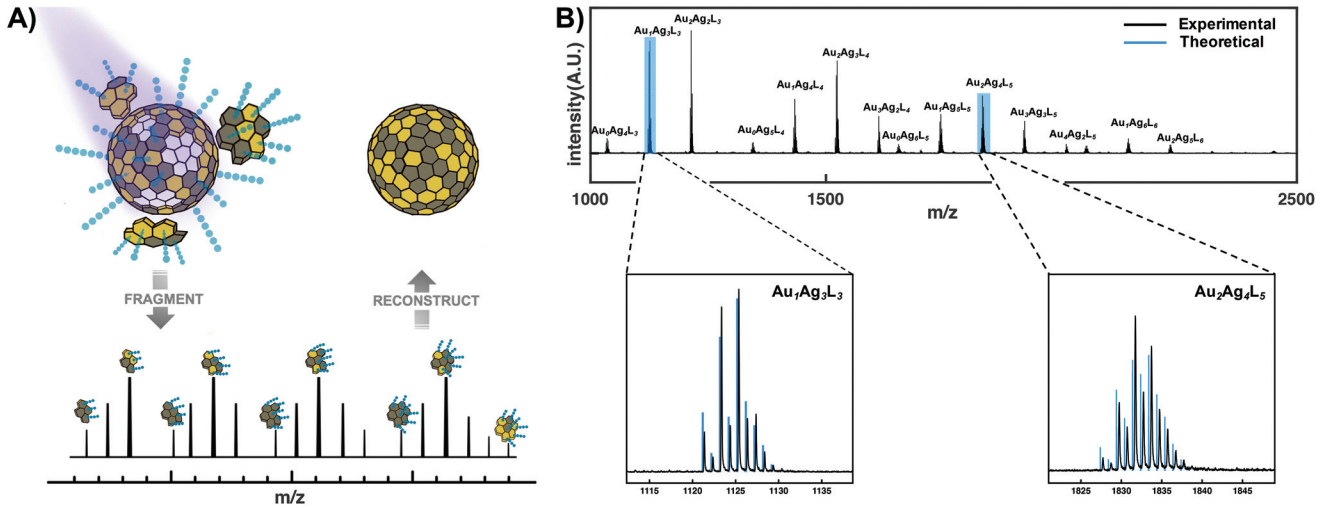

Fig. 1 (A) Schematic illustration of the workflow: surface fragmentation, peak analysis and reconstruction; (B) representative MALDI mass spectrum of DDT AuAg NPs, with the insets comparing the highly-resolved experimental isotopic distribution with the theoretical prediction to assist in peak assignment. All fragments follow the chemical formula $(Au_xAg_{n-x})L_{n-1}$ (n is the sum number of Au and Ag atoms in the fragments; L denotes the ligands; x is the number of Au atoms and $0 \leq x \leq n$).

ment of the MALDI peaks is ensured by matching the experimental m/z ratio to the predicted monoisotopic value and comparing theoretical and experimental isotope patterns (ESI, Table. S1†).

In Table S2 (ESI)† there are all the integrated signals for the peaks found in the MALDI-TOF spectra acquired. We have made the assumption that such integrals are proportional to the relative abundance of the corresponding fragments. This assumption is justified by the studies reported in the literature that have related the relative abundance of mixed-ligand fragments calculated using MALDI-TOF integrated signals with that found using NMR.[33,37] Consequently, the fraction of Au atoms on the surface of the nanoparticles was calculated as the weighted average of its relative abundance in the MALDI fragments (Equation in Experimental). To check for internal consistency, we applied this data processing to the three detectable fragment types separately (n = 5, or 6, or 7). We found very good consistency for these independent calculations with the maximum error being 1.7%.

To compare the surface composition of the nanoparticles with the bulk composition, we performed inductively coupled plasma mass spectrometry (ICP-MS) on all five particles studied, as ICP-MS is known to accurately measure the bulk composition of the nanoparticles.[38–40] X-ray Photoelectron Spectroscopy (XPS) was also applied as a complementary technique. The results are shown in Table 1. It is immediately evident that the nanoparticle composition is different from the stoichiometric ratio used in the reaction and the particles are enriched in Au. We then performed MALDI-TOF to calculate the surface composition. For clear visual comparison of the five samples, only peaks from n = 5 are shown in Fig. 2A. In Fig. 2B we show a comparison between the composition of the bulk of the nanoparticles as measured *via* ICP-MS and the surface composition measured by MALDI.

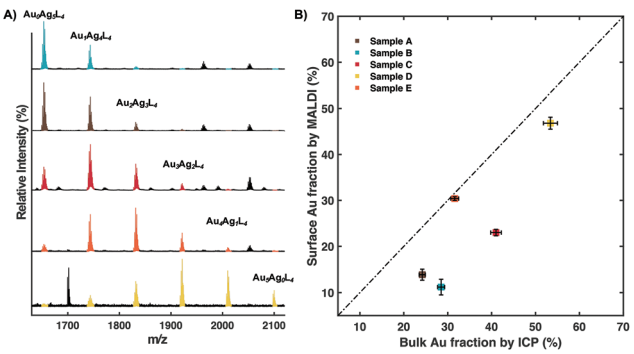

Fig. 2 Surface enrichment of Ag atoms is identified for the majority of our AuAg NPs. Varying the relative feeding amount of the two metallic precursors results in a series of batches with various surface compositions; shown topdown in (A) are peaks (color-coded) from $(AuAg)_5L_4$ fragments with peaks from other n (in black) hidden for image clarity. (B) Surface Au fraction by MALDI is plotted against bulk Au fraction characterized by ICP-MS (the error bar is reported as 2% of the experimental result) to show surface enrichment of Ag.

All points in the graph shown in Fig. 2B are below the line of equal composition indicating a surface enrichment in Ag. So while Au is enriched in the nanoparticles compared to the stoichiometric ratio, the surface of the nanoparticles is enriched in Ag compared to the bulk. The overall enrichment in Au for the nanoparticles could be explained by the fact that Au(III) has a higher reduction potential compared to Ag(I), thus it will be preferentially reduced to form the core of the particles. The surface of the nanoparticles may be enriched in Ag either because of surface energy considerations or just being kinetically trapped at a composition closer to the stoichiometric one. In fact, it has been stated that, upon the formation of AuAg bimetallic nanoparticles, Ag atoms migrate towards

the surface by Au–Ag interdiffusion to minimize the surface energy.[24,41]

MALDI-TOF analysis allows to further investigate the surface arrangement of the Ag and Au atoms by comparison of the distribution of the signal intensities with the binomial distribution expected for a random mixture of the two atoms. A quantitative analysis of the data produced was performed by calculating the SSR value of all the distribution obtained for each particle at each n. First, we calculated all binomial distributions applying the surface composition as the probability. In Fig. 3A, the measured abundance of the $(Au_xAg_{n-x})L_{n-1}$ fragments is reported for three different values of n (from top to bottom n = 5/6/7). For example, the top graph shows the case for n = 5. The measured abundance (triangle) is compared to the ideal binomial distribution abundance (cross). The SSR is derived by comparing these two distributions. For all five samples, the SSR values were calculated at each n and plotted against the surface composition as shown in Fig. 3B. The spread between the data achieved for a fixed surface composition but different n should serve as a generic indication of the uncertainty correlated with this SSR approach to interpret the data. By comparing our results to the threshold SSR value previously reported for random distribution (ref. 26), one could conclude that Sample B is the only one that has an SSR above the random distribution. Nevertheless, there is a lot of subjectivity in determining the threshold, as such a better approach is to solve the surface structure using Monte-Carlo type approach as discussed below.

A more unbiased approach to interpret the data is the use of a bead model to fit the globality of the data (not just data at a single n) *via* a Monte-Carlo-type simulation. This concept

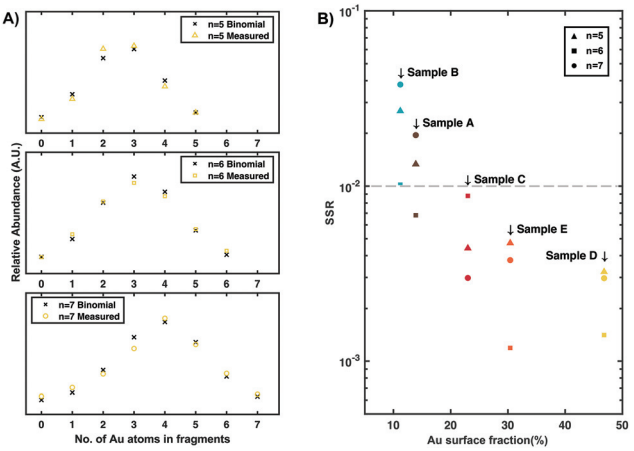

Fig. 3 Statistic deviation from randomness serving as semi-quantitation of surface phase separation. (A) For each set of data, SSR values between measured relative peak intensities (from various fragment types n = 5, triangle; n = 6, square; n = 7, circle) and binomial distribution coefficients are calculated as statistic distance of the sample surface from random arrangement. (B) SSR values follow a trend of decreasing as Au and Ag surface fractions approach equivalent, indicating an associating effect to lower the overall surface energy. (The dashed line stands for the SSR threshold value for random distribution.)

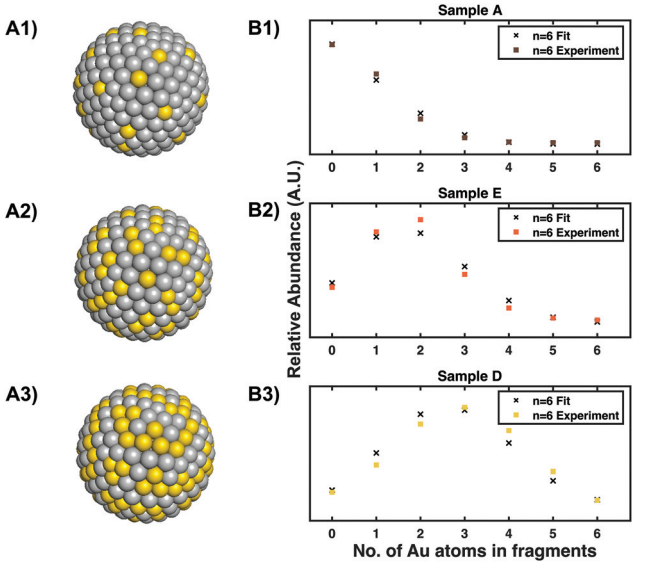

Fig. 4 Monte Carlo simulation to reconstruct the surface morphology. Starting from a Janus-type surface, three datasets (from Sample A, E and D) featuring various compositions are simulated with a Monte Carlo simulation to reconstruct the sample surface. The reconstructed models are shown as A1), A2) and A3) together with the fitting quality shown in the panel to the right, for Sample A, E and D, respectively.

was first proposed in our previous work on binary ligand shells.[33] First we generate an icosphere with a certain number of surface nodes to match the actual size, *e.g.* 252 nodes considering the dimension of our samples; then these surface nodes are assigned to be 50 : 50 Janus by the computer as the starting point; to initiate an iteration, the assignment of a random site is reversed to generate a temporary model; next, two mass spectra are simulated based on the two model to compare; the model whose statistical distance (by comparing SSR) is closer to the experimental spectrum will be accepted for the iteration step. The process examines as many possibilities with a sufficient amount of iterations (usually ~10 000 times) until the SSR reaches a plateau. Eventually, the output model is regarded as an average representative of the surface morphology for the whole batch. In Fig. 4, three experimental mass spectra are simulated and in the right column, experimental and simulated peak signals from the fragment type n = 6 are plotted to show the fitting quality. Our data clearly show a random distribution of the Ag and Au atoms at the surface of the nanoparticles.

Discussion

Further investigations should be conducted to generalize this tool. Herein we name a just a few based on our experimental experiences. We would like to point out two features of a potential good matrix for this application. The first feature is low ionization energy, a key thermochemical characteristic that's beneficial to the overall softness. The second feature is

high electron affinity.[42,43] We have reached this conclusion because we have noticed a wide use of DCTB (for hydrophobic analytes) and CHCA (for hydrophilic analytes) for nanoparticles. Both matrix materials work under the electron transfer process where the analyte fragments are electron donor and forms positive ions. One key aspect is the versatility of ionizable elements. We tried DDT protected Pd, Pt, PdAu and AgPt nanoparticles, together with various commercially available matrix materials. Unfortunately, the AuAgDDT-like fragments were not observed. Another layer of versatility involves the types of ligands. Will nanoparticles covered with other types of ligands behave similarly under MALDI? Regarding the structural factors of the metallic cores, we should try to understand if there's a specific size range where the nanoparticle could be characterized. When this technique is applied onto non-spherical nanoparticles, variation in ionization efficiency due to the structural heterogeneity should be further addressed.

Conclusions

In summary, using DDT coated AuAg bimetallic nanoparticles we have demonstrated that MALDI-TOF is a promising tool to characterize the composition and the arrangement of surface atoms of bimetallic nanoparticles. Despite the challenges mentioned above, MALDI is a dynamic field and with new matrix materials being discovered, the method presented here could become one of the standards for characterizing in multicomponent nanoparticles.

Experimental

Materials

For nanoparticle synthesis, gold(III) chloride trihydrate, silver trifluoroacetate, 1-dodecanethiol (DDT) and borane *tert*-butylamine complex were purchased from Sigma-Aldrich and used as received.

For MALDI sample preparation, 2-[(2*E*)-3-(4- *tert*-butylphenyl)-2-methylprop-2-enylidene] malononitrile (DCTB) and 9-nitroanthracene (9-NA) were purchased from Sigma-Aldrich and used as received.

Nanoparticle synthesis and purification

For the Au feeding ratio of 50%, 0.2 mmol $HAuCl_4{\cdot}3H_2O$ and 0.2 mmol CF3COOAg (together with 0.4 mmol DDT) were separately dissolved in 10 ml chloroform and sonicated for 3 minutes. 4 mmol borane *tert*-butylamine complex were dissolved in 20 ml chloroform as reducing agent. Once the oil bath reached 50 °C, both Au and Ag precursor solutions were added into a 100 ml round-bottom flask. After stirring for ~3 minutes, reducing agent was added and the reaction mixture was left for 2 hours before collection. To quench the reaction, heating was turned off and the reaction mixture naturally cooled down to room temperature. The insoluble by-product was then removed by centrifugal precipitation.

MALDI-TOF sample preparation and measurement

All the measurements were conducted using a Bruker AutoFlex Speed instrument. AuAg nanoparticles/chloroform solution (10 mg ml^{-1}) were prepared and then mixed with an equal volume of matrix/chloroform solution (the matrix material DCTB or 9-NA at concentration of 25 mg ml^{-1}). 2 μl aliquot of such NP-matrix mixture were deposited onto a stainless steel target plate to co-crystalize. Measurements were performed under reflector positive mode in the range of 700–3500 *m*/*z*. The laser (355 nm Smartbeam Nd:YAG-laser) intensity was kept at ~30% if DCTB was applied as matrix, or ~60% if 9-NA was used. (Control measurements were made on the same sample with the two matrix materials and we found non-significant difference.)

Calculation of Au surface fraction θ:

$$\theta = \sum_{i=0}^{n} (i/n)^{*}P_i \quad \text{with} \quad P_i = \frac{n_i}{\sum_{i=0}^{n} n_i}$$

n – fragment type n in $(AuAg)_nL_{n-1}$; n_i – the intensity of fragment $Au_iAg_{n-i}L_{n-1}$ with i Au atoms; P_i – relative abundance of the fragment $Au_iAg_{n-i}L_{n-1}$; θ – Au surface fraction in the fragment type n.

Conflicts of interest

There are no conflicts to declare.

Acknowledgements

This project received funding from the Swiss National Foundation. The authors are grateful to Dr Natalia Gasilova (ISIC-EPFL) for her help in ICP-MS and grateful to Dr. Reza Zamani (CIME-EPFL) for valuable discussions. We thank Mr Matteo Gasbarri for his help with TEM imaging.

References

1 H. Liao, A. Fisher and Z. J. Xu, *Small*, 2015, **11**, 3221–3246.
2 A. K. Singh and Q. Xu, *ChemCatChem*, 2013, **5**, 652–676.
3 J. Rick, M.-C. Tsai and B. J. Hwang, *Nanomaterials*, 2016, **6**, 5.
4 R. Mandal, A. Baranwal, A. Srivastava and P. Chandra, *Biosens. Bioelectron.*, 2018, **117**, 546–561.
5 B. W. Boote, H. Byun and J.-H. Kim, *J. Nanosci. Nanotechnol.*, 2014, **14**, 1563–1577.
6 P. Srinoi, Y.-T. Chen, V. Vittur, M. D. Marquez and T. R. Lee, *Appl. Sci.*, 2018, **8**, 1106.
7 J. Suntivich, Z. Xu, C. E. Carlton, J. Kim, B. Han, S. W. Lee, N. Bonnet, N. Marzari, L. F. Allard, H. A. Gasteiger, K. Hamad-Schifferli and Y. Shao-Horn, *J. Am. Chem. Soc.*, 2013, **135**, 7985–7991.

8 T. J. A. Slater, A. Macedo, S. L. M. Schroeder, M. G. Burke, P. O'Brien, P. H. C. Camargo and S. J. Haigh, *Nano Lett.*, 2014, **14**, 1921–1926.
9 K. J. J. Mayrhofer, K. Hartl, V. Juhart and M. Arenz, *J. Am. Chem. Soc.*, 2009, **131**, 16348–16349.
10 C. L. Bracey, P. R. Ellis and G. J. Hutchings, *Chem. Soc. Rev.*, 2009, **38**, 2231–2243.
11 G. Liao, J. Fang, Q. Li, S. Li, Z. Xu and B. Fang, *Nanoscale*, 2019, **11**, 7062–7096.
12 J. H. Lee, S. Kattel, Z. Jiang, Z. Xie, S. Yao, B. M. Tackett, W. Xu, N. S. Marinkovic and J. G. Chen, *Nat. Commun.*, 2019, **10**, 1–8.
13 D. Ren, J. Gao, L. Pan, Z. Wang, J. Luo, S. M. Zakeeruddin, A. Hagfeldt and M. Grätzel, *Angew. Chem., Int. Ed.*, 2019, **58**, 15036–15040.
14 J. Huang and R. Buonsanti, *Chem. Mater.*, 2019, **31**, 13–25.
15 D. Kim, C. Xie, N. Becknell, Y. Yu, M. Karamad, K. Chan, E. J. Crumlin, J. K. Nørskov and P. Yang, *J. Am. Chem. Soc.*, 2017, **139**, 8329–8336.
16 C. Cui, L. Gan, M. Heggen, S. Rudi and P. Strasser, *Nat. Mater.*, 2013, **12**, 765–771.
17 V. R. Stamenkovic, B. S. Mun, M. Arenz, K. J. J. Mayrhofer, C. A. Lucas, G. Wang, P. N. Ross and N. M. Markovic, *Nat. Mater.*, 2007, **6**, 241–247.
18 A. Wang, J. Li and T. Zhang, *Nat. Rev. Chem.*, 2018, **2**, 65–81.
19 J. Huang, M. Mensi, E. Oveisi, V. Mantella and R. Buonsanti, *J. Am. Chem. Soc.*, 2019, **141**, 2490–2499.
20 G. Guisbiers, R. Mendoza-Cruz, L. Bazán-Díaz, J. J. Velázquez-Salazar, R. Mendoza-Perez, J. A. Robledo-Torres, J.-L. Rodriguez-Lopez, J. M. Montejano-Carrizales, R. L. Whetten and M. José-Yacamán, *ACS Nano*, 2016, **10**, 188–198.
21 L. Deng, W. Hu, H. Deng, S. Xiao and J. Tang, *J. Phys. Chem. C*, 2011, **115**, 11355–11363.
22 J. Timoshenko, C. J. Wrasman, M. Luneau, T. Shirman, M. Cargnello, S. R. Bare, J. Aizenberg, C. M. Friend and A. I. Frenkel, *Nano Lett.*, 2019, **19**, 520–529.
23 E. A. Lewis, T. J. A. Slater, E. Prestat, A. Macedo, P. O'Brien, P. H. C. Camargo and S. J. Haigh, *Nanoscale*, 2014, **6**, 13598–13605.
24 G. Guisbiers, S. Mejia-Rosales, S. Khanal, F. Ruiz-Zepeda, R. L. Whetten and M. José-Yacaman, *Nano Lett.*, 2014, **11**, 6718–6726.
25 K. M. Harkness, L. S. Fenn, D. E. Cliffel and J. A. McLean, *Anal. Chem.*, 2010, **82**, 3061–3066.
26 K. M. Harkness, A. Balinski, J. A. McLean and D. E. Cliffel, *Angew. Chem., Int. Ed.*, 2011, **50**, 10554–10559.
27 A. Dass, K. Holt, J. F. Parker, S. W. Feldberg and R. W. Murray, *J. Phys. Chem. C*, 2008, **112**, 20276–20283.
28 S. N. Merz, Z. J. Farrell, C. J. Dunn, R. J. Swanson, S. A. Egorov and D. L. Green, *ACS Nano*, 2016, **10**, 9871–9878.
29 S. N. Merz, Z. J. Farrell, J. Pearring, E. Hoover, M. Kester, S. A. Egorov, D. L. Green and K. H. DuBay, *ACS Nano*, 2018, **12**, 11031–11040.
30 Z. Farrell, S. Merz, J. Seager, C. Dunn, S. Egorov and D. L. Green, *Angew. Chem., Int. Ed.*, 2015, **54**, 6479–6482.
31 S. N. Merz, E. Hoover, S. A. Egorov, K. H. DuBay and D. L. Green, *Soft Matter*, 2019, **15**, 4498–4507.
32 Z. Luo, J. Hou, L. Menin, Q. K. Ong and F. Stellacci, *Angew. Chem.*, 2017, **129**, 13706–13710.
33 Z. Luo, Y. Zhao, T. Darwish, Y. Wang, J. Hou and F. Stellacci, *Nat. Commun.*, 2018, **9**, 4478.
34 Z. Farrell, S. Merz, J. Seager, C. Dunn, S. Egorov and D. L. Green, *Angew. Chem., Int. Ed.*, 2015, **54**, 6479–6482.
35 N. Zheng, J. Fan and G. D. Stucky, *J. Am. Chem. Soc.*, 2006, **128**, 6550–6551.
36 M. Karas and F. Hillenkamp, *Anal. Chem.*, 1988, **60**, 2299–2301.
37 K. M. Harkness, B. C. Hixson, L. S. Fenn, B. N. Turner, A. C. Rape, C. A. Simpson, B. J. Huffman, T. C. Okoli, J. A. McLean and D. E. Cliffel, *Anal. Chem.*, 2010, **82**, 9268–9274.
38 P. Mani, R. Srivastava and P. Strasser, *J. Power Sources*, 2011, **196**, 666–673.
39 G. Behmenyar and A. N. Akın, *J. Power Sources*, 2014, **249**, 239–246.
40 W. Li, L. Kuai, Q. Qin and B. Geng, *J. Mater. Chem. A*, 2013, **1**, 7111–7117.
41 T. Shibata, B. A. Bunker, Z. Zhang, D. Meisel, C. F. Vardeman and J. D. Gezelter, *J. Am. Chem. Soc.*, 2002, **124**, 11989–11996.
42 S. G. Kotsiris, *et al.*, *Eur. J. Mass Spectrom.*, 2006, **12**, 397–408.
43 Y. V. Vasil'ev, *et al.*, *J. Phys. Chem. A*, 2006, **110**, 5967–5972.